Manuscript prepared for Atmos. Meas. Tech.
with version 2014/09/16 7.15 Copernicus papers of the LaTeX class copernicus.cls.
Date: 11 October 2016

Intra-pixel variability in satellite NO_2 measurements

Stephen Broccardo[1], Klaus-Peter Heue[2], David Walter[3], Christian Meyer[4], Alexander Kokhanovsky[5], Ronald v.d. A[6], Kristy Langermann[7], Stuart Piketh[8], and Ulrich Platt[9]

[1]School of Geography, Archaeology and Environmental Science, University of the Witwatersrand, Johannesburg, 2030, South Africa, *now at* Unit for Environmental Science and Management, North-West University, Potchefstroom, 2531, South Africa
[2]DLR Earth Observation Center, Oberpfaffenhofen, 82234 Wessling, Germany
[3]Max Planck Institute for Chemistry, Hahn-Meitner-Weg 1, 55128 Mainz, Germany
[4]Zentrum Mikroelektronik Dresden AG, Grentzstr 28, 01109 Dresden, Germany
[5]EUMETSAT, Eumetsat Allee 1, 64295, Darmstadt, Germany *and* Moscow Engineering Physics Institute, National Research Nuclear University, Kashirskoe Ave. 31, 115409, Moscow, Russia
[6]R&D Satellite Observations, KNMI, Utrechtseweg 297, 3731GA, De Bilt, Netherlands
[7]Eskom Holdings SOC Ltd, Megawatt Park, Maxwell Drive, Sandton, 2157, South Africa
[8]Climatology Research Group, North-West University, Potchefstroom, 2531, South Africa
[9]Institut für Umweltphysik, Im Neuenheimer Feld 229, 69120, Heidelberg, Germany

Correspondence to: S. Broccardo (sbroccardo@gmail.com)

Abstract. Aircraft measurements of NO_2 using a differential optical absorption spectrometer (DOAS) instrument over the South African Highveld region in August 2007 are presented. In-situ aerosol and trace-gas vertical profile measurements, along with aerosol optical thickness and single-scattering albedo from AERONET, are used to devise scenarios for a radiative-transfer modelling sensitivity study. Uncertainty in the air-mass factor due to variations in profile shape is constrained, and used to calculate vertical column densities, which are compared to co-located satellite measurements. The lower spatial resolution of the satellites cannot resolve the detailed plume structures revealed in the aircraft measurements. The airborne DOAS in general measured steeper horizontal gradients and higher peak NO_2 VCD. Spatially-averaged aircraft measurements close to major sources indicate NO_2 column densities more than twice those measured by the satellite. The agreement between the high-resolution aircraft instrument and the satellite instrument improves with distance from the source. Despite the low resolution, satellite images reveal point sources and plumes that retain their structure for several hundred kilometers downwind.

1 Introduction

Space-based measurements of trace-gases are increasingly being used to monitor tropospheric air pollution (McLinden et al., 2012; Streets et al., 2013), including the identification of major sources missing from public emissions inventories (Mclinden et al., 2016) and the quantification of source strengths (Beirle et al., 2011). Satellite observations have highlighted the South African Highveld as a region with a higher than expected concentration of NO_2 (Martin et al., 2002; Toenges-Schuller et al., 2006), and with an increasing trend (Richter et al., 2005; van der A et al., 2008). To further investigate this phenomenon, a high-resolution imaging differential optical absorption spectrometer (iDOAS) was flown on board the South African Weather Service Aerocommander 690A research aircraft during a dry-season flight campaign over the Highveld in 2007. Results from research flights conducted on the 9th, 11th, 14th and 18th of August 2007 are presented. Aircraft vertical profile measurements of NO_y and aerosols are used to devise several representative scenarios of the vertical distribution of these two species, and a sensitivity study is performed using the SCIATRAN radiative transfer model to constrain the uncertainty in the air-mass factor. Measurements from the nadir pixel of the iDOAS are compared with operational satellite measurements of NO_2 from OMI (Ozone Monitoring Instrument) and SCIAMACHY (SCanning Imaging Absorption spectroMeter for Atmospheric CHartographY) made on the same day.

The Highveld is a high-altitude plateau in the interior of South Africa (Fig. 1), home to the Johannesburg-Pretoria conurbation and the adjoining industrial towns of Ekuruleni to the east and Vereeniging and Vanderbijlpark to the south. The latter two along with the petrochemical industry and town at Sasolburg enclose an area known as the Vaal Triangle. The Vaal Triangle is also home to two steelmills and a coal-fired power station. To the east of Johannesburg, at Secunda, there is a coal-to-fuel (Fischer-Tropsch process) synfuel refinery, which also generates electricity from coal. Secunda is situated in a region often referred to as the Eastern Highveld or Mpumalanga Highveld; this region is also home to eleven more coal-fired power stations, and several steel-mills. Analysis of a year of ground-based monitoring station data by Collett et al. (2010) indicates that most of the NO_2 on the Highveld is from tall-stack industrial emissions, and has an impact on surface ozone concentrations (Balashov et al., 2014). A combined analysis of satellite and ground-based measurements indicates that the conurbation of greater Johannesburg is also a significant source of NO_2 (Lourens et al., 2012). In between the heavy industries are coal mines to supply fuel to the former, a small town about every hundred kilometers, and farmland or grassland. The Highveld is impacted by biomass-burning sources in the winter season; along with the urban and industrial sources of trace-gases and aerosols, it forms a natural laboratory isolated on a global scale from nearby sources, and controlled by synoptic-scale meteorology (Annegarn et al., 2002).

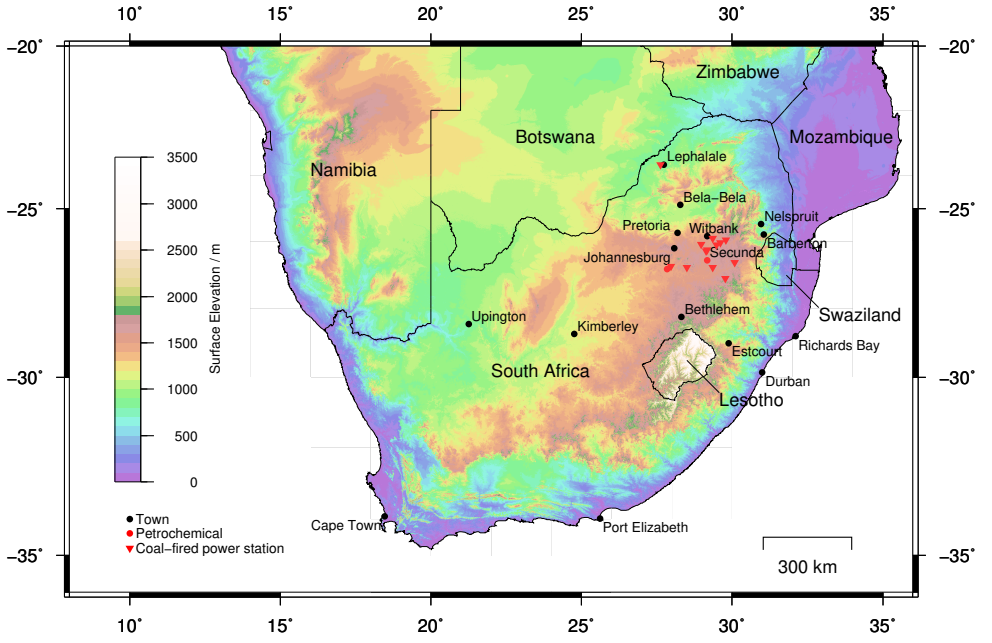

Figure 1. A map of Southern Africa, showing the high-altitude plateau of the Highveld to the east of Johannesburg, and the cluster of coal-fired power stations and heavy industries on the eastern Highveld. The coal-fired power station at Lephalale is indicated. Power stations not shown here include smaller coal-fired and gas-turbine power stations operated by the cities.

2 Measurements and Methods

The measurement principle employed to observe NO_2 from satellite, and from our airborne iDOAS instrument is that of differential optical absorption spectroscopy (DOAS), described by Platt and Stutz (2008). As with any absorption spectroscopy technique, the magnitude of the measured quantity depends on the path length, p, through the absorber and the concentration, $c(p)$, of the absorber. In the case of measurements made in the atmosphere using sunlight, the DOAS analysis yields a slant column density (SCD), S:

$$S = \int_{path} c(p)dp \tag{1}$$

This name reflects the fact that the light path through the atmosphere is not known *a-priori*, and to a first approximation, is slanted. A more useful quantity is the vertical column density (VCD), which is the concentration of the absorber integrated along a vertical path between the earth's surface and the top of the atmosphere. In the standard DOAS formulation suited to measurement of relatively small slant-column densities (Rozanov and Rozanov, 2010), these two quantities are related by the air-mass factor (AMF):

$$A = S/V \tag{2}$$

Where A is the air-mass factor, V is the vertical column density and S is the slant column density as before.

A DOAS instrument based on an imaging spectrograph employing a pushbroom viewing geometry was fitted into the Aerocommander 690A, and slant-column densities were retrieved using the WinDOAS software package, as described in more detail by Heue et al. (2008). In addition to the imaging DOAS (iDOAS) instrument, the aircraft carried a Particle Measurement Systems Passive Cavity Aerosol Spectrometer Probe 100X (PCASP), operated with the pre-heater switched on; and a Thermo Scientific 42i instrument with a molybdenum converter in the cabin, plumbed into the aircraft's scientific-air inlet in order to measure in-situ $\mathrm{NO_y}$. An instrument with a photolytic converter to measure $\mathrm{NO_2}$ was not within the project's budget. The aircraft is fitted with a Rosemount ambient temperature sensor, and a separate pitot-static system for measurement and logging of static and dynamic pressure. The humidity sensor fitted to the aircraft did not function during this campaign. The aircraft's data aquisition system also logged parameters from a GPS (Global Positioning System) receiver.

Satellite-based measurements of $\mathrm{NO_2}$ were made operationally from the SCIAMACHY (Scanning Imaging Absorption spectroMeter for Atmospheric CHartographY) instrument on board the European Space Agency (ESA) ENVISAT satellite from March 2002 to April 2012; and from OMI (Ozone Monitoring Instrument) on the National Aeronautics and Space Agency (NASA) Aura satellite from October 2004 until the present. The SCIAMACHY instrument operated in a whiskbroom geometry with eight measurement channels covering the spectral range from $214\mathrm{nm}$ to $2386\mathrm{nm}$. The ENVISAT satellite orbited at a mean altitude of $799.8\mathrm{km}$ with an orbital period of $100.6\mathrm{min}$ and a repeat cycle of 35 days. Overpass time on the Highveld was around 10:00 local time. In the nadir viewing geometry the ground pixel size is $60\mathrm{km}$ by $30\mathrm{km}$, and global coverage was achieved every 6 days (Gottwald et al., 2006). The AURA satellite orbits at a mean altitude of $709\mathrm{km}$, with an orbital period of $98.8\mathrm{min}$ and a repeat cycle of 16 days. The OMI instrument measures wavelengths between $270\mathrm{nm}$ and $500\mathrm{nm}$ in pushbroom geometry with a nadir ground-pixel size of $24\mathrm{km}$ by $13\mathrm{km}$ (Levelt et al., 2006). Overpass on the Highveld is around 14:00 local time.

Measurements from the nadir pixel of the iDOAS are compared with $\mathrm{NO_2}$ tropospheric VCD from the DOMINO version 2.0 product from the OMI instrument (Boersma et al., 2011) available from http://www.temis.nl. *A-priori* vertical profiles of $\mathrm{NO_2}$ from the TM4 global chemistry-transport model (Dentener et al., 2003) are used to calculate tropospheric air-mass factors, and stratospheric $\mathrm{NO_2}$ is estimated by assimilation of slant columns in the TM4 model. The TM4NO2A product (also available from http://www.temis.nl) uses a similar scheme, however slant column measurements from the SCIAMACHY instrument are used.

Flights were planned to approximately follow the nadir track of the satellite (carrying OMI or SCIAMACHY) that would be passing over the Highveld on the day, with the aircraft flying nominally at $6000\mathrm{m}$ above sea level, the actual altitude varying by $1000\mathrm{ft}$ ($312\mathrm{m}$) as demanded by

air-traffic rules. Over much of the Highveld, this would be approximately $4500\mathrm{m}$ above the ground, giving a ground pixel size from the iDOAS around $80\mathrm{m}$ (Heue et al., 2008).

At the beginning and end of the satellite-tracking segment of each flight, a vertical profile measurement was performed. Vertical profiles were started and ended as low as safety allowed, judged visually to be around $400\mathrm{m}$–$500\mathrm{m}$ above ground level (AGL). The lower altitude limit of vertical profile measurements could be extended to the surface if the profiles were flown overhead a suitable airfield, and the aircraft performed a missed-approach procedure. This will limit the choice of locations for vertical profile measurements, but the quality of the profiles would be improved by extending the measurements down to ground level. Intermittent failures of the PCASP probe and the data aquisition system detract from the usefulness of some of the profiles, and these partial profiles are not presented here. Aerosol number concentration and in-situ $\mathrm{NO_y}$ are averaged into $50\mathrm{m}$ altitude bins, temperature into $20\mathrm{m}$ bins. Altitude intervals of interest are identified by inspection of the vertical profile measurements, and average particle size spectra are calculated. No corrections for aerosol refractive index are made, since the present measurements are not used for determination of radiative properties of the aerosols.

Monthly statistics are calculated for the late-winter season from measurements of aerosol optical thickness (AOT) and single-scattering albedo (SSA or ϖ) taken from an AERONET sun-photometer (Holben et al., 2001) that was situated at the University of the Witwatersrand in Johannesburg during 2007 and 2009. The aircraft vertical profile measurements and sun-photometer measurements are used as guidance in creating a number of vertical profile scenarios of aerosols and $\mathrm{NO_2}$; which are used in a model sensitivity study using the SCIATRAN radiative transfer model (RTM) (Rozanov et al., 2014). The results of this sensitivity study are used to constrain the uncertainty in the air-mass factor for the iDOAS $\mathrm{NO_2}$ measurements.

Two approaches are taken in order to allow a comparison with the satellite-based measurements: the first is to average high-resolution iDOAS measurements using a ten-second moving average in order to smooth out fine-spatial-scale variations and make a comparison with the much larger satellite pixels. With the aircraft's ground speed being around $120\mathrm{m\,s^{-1}}$, on a spatial scale this time-based moving-average is over approximately $1.2\mathrm{km}$. The second approach is to calculate the mean and standard deviation of all iDOAS measurements within a satellite ground pixel to compare with the value from the satellite tropospheric $\mathrm{NO_2}$ product for that pixel.

3 Aircraft Vertical Profile Measurements

From the measured vertical profiles, several features can be discerned:

1. NO_y and aerosol concentration profile shapes are usually block-shaped or exponentially-decreasing with altitude.

Since aerosol particles or their precursors, and NO_y, often are emitted from the same surface urban, industrial or biomass-burning sources, the patterns of their dispersal will be similar. A block-shaped vertical profile can be expected under conditions where turbulent mixing causes vertical dispersion in the planetary boundary layer, an exponentially-decreasing profile will occur under conditions of greater atmospheric stability.

2. There are frequently elevated layers of enhanced aerosol and NO_y concentration, isolated from the planetary boundary layer by a layer of cleaner air.

Swap and Tyson (1999) assess vertical mixing and transport of air parcels between spatially and temporally persistent stable layers over the sub-continent. These stable layers around $850\mathrm{hPa}$ (in coastal areas), $700\mathrm{hPa}$, $500\mathrm{hPa}$, and $300\mathrm{hPa}$ lead to peaks and discontinuities in the vertical profile of trace-gases and aerosols. Published vertical profile measurements of aerosol scattering coefficient (Magi et al., 2003) and particle concentration (Hobbs, 2003; Swap and Tyson, 1999) from the sub-continent show features consistent with this generalization.

3. The aerosol size distribution is consistent in the lower and upper sections the profile

Since the aerosols in the elevated layers are transported there from the lower layers (Swap and Tyson, 1999; Hobbs, 2003) where they are emitted or formed, the size distributions can be expected to be similar. This similarity in aerosol size distribution through the vertical profile was also found in measurements over Namibia (Haywood, 2003a, b), a region frequently under the influence of the same sub-continental-scale air transport regime as the Highveld (Swap and Tyson, 1999). Assuming that aerosol optical properties are the same in the elevated layers as they are near the surface, similar size distributions mean that the aerosol scattering and absorption coefficients will be proportional to aerosol number concentration. These generalizations of the vertical profile are used to develop scenarios for a radiative transfer modelling sensitivity study described below.

As examples of aircraft vertical profile measurements, the profile overhead Richards Bay measured on 11 August is shown in Fig. 2 and the profile overhead Nelspruit on the same day is shown in Fig. 3. Extrapolating the available measurements to the surface at Richard's Bay, the aerosol number and NO_y concentrations appear to follow a generally exponentially-decreasing profile with height. The top of this exponential profile is at the bottom of a temperature inversion around $1750\mathrm{m}$ (approximately $815\mathrm{hPa}$). Embedded within this profile there is a layer of elevated NO_y between $700\mathrm{m}$ and $1000\mathrm{m}$; this layer of enhanced NO_y concentration is approximately mirrored in the aerosol profile.

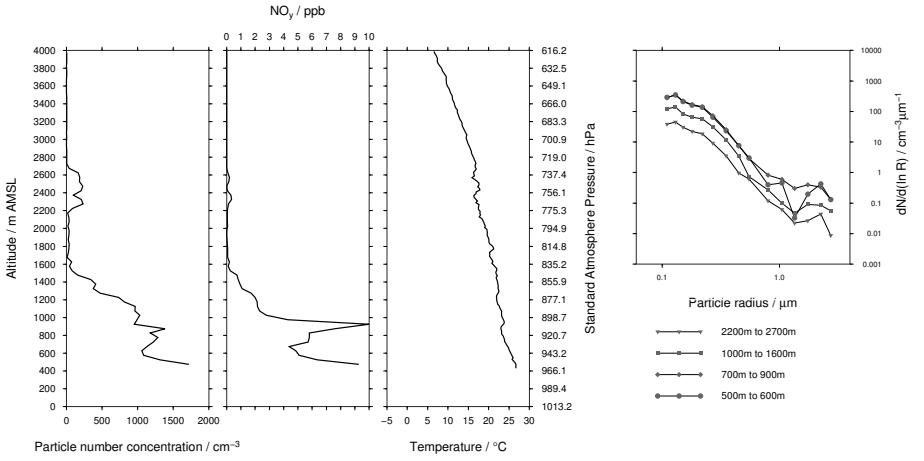

Figure 2. Vertical profiles of particle number concentration, in-situ NO_y and temperature on 11 August 2007 between 11:01 and 11:40 UTC overhead Richards Bay. Average particle size spectra for altitude intervals of interest are plotted.

In addition to the exponentially-decreasing profile close to the ground there is a separate elevated layer of enhanced aerosol and NO_y, between 2200m and 2700m above sea level, capped by another temperature inversion at approximately 2700m (730hPa). Layer-averaged aerosol size spectra from the altitude intervals 500m–600m, 700m–900m, 1000m–1600m, and 2200m–2700m indicate a similarly-shaped bimodal lognormal distribution in all cases, with modes at 0.13µm and 2.25µm.

Over Nelspruit (Fig. 3), the aircraft descended through a plume between 2900m–2500m, observed to originate from a large forest-fire nearby; NO_y concentrations up to 35ppb and aerosol number concentrations greater than 6000cm^{-3} were measured in this plume. This large plume was trapped under a temperature inversion at 2900m AMSL (approximately 710hPa). Below this, between 2400m–2100m a layer of enhanced aerosol number concentration, and NO_y concentration was found. From the bottom of this layer to the ground (the aircraft landed at Nelspruit to re-fuel), the NO_y concentration remains approximately constant, and the particle number concentration shows some variations, but in general a block-shaped vertical profile is found. Aerosol size spectra for the intervals between and 900m–1800m, 1800m–2000m and 2000m–2400m indicate a bimodal lognormal size distribution with the modes of the distribution at 0.13µm and 2.0µm.

Seventy-two hour Hysplit (Stein et al., 2015) back-trajectories (not shown here) indicate that the air measured in these profiles had re-circulated over Mozambique, southern Zimbabwe and south-eastern Botswana before making its way in a south-easterly direction towards either Richards Bay or Nelspruit.

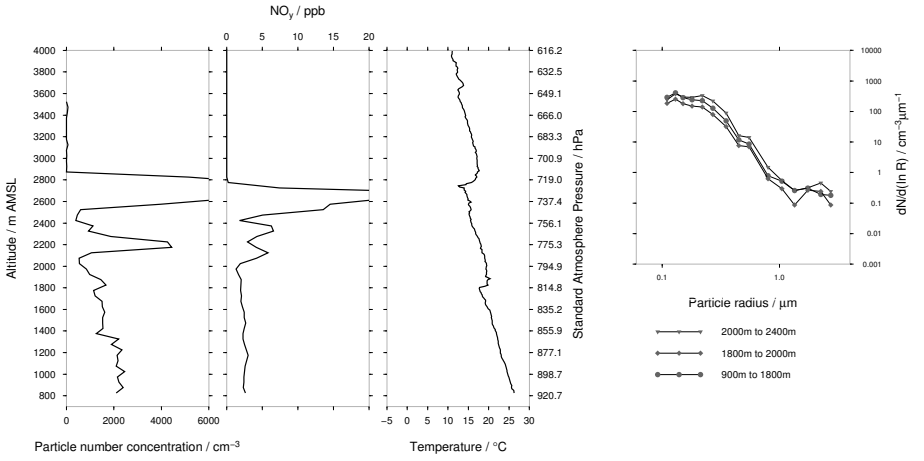

Figure 3. Vertical profiles of particle number concentration, in-situ NO_y and temperature on 11 August 2007, overhead Nelspruit between 12:40 and 13:20 UTC. Average particle size spectra for altitude intervals of interest are plotted.

4 Radiative Transfer Modelling and Airmass Factor Calculation

Leitão et al. (2010) highlight the importance of including aerosols in the calculation of the air-mass factor (AMF, defined in Section 2). In that study, several vertical profile scenarios are devised from chemistry-transport model output. For the present study, idealised scenarios representative of the Highveld are used to perform a sensitivity study using the SCIATRAN radiative transfer model (Rozanov et al., 2014). Our scenarios are based on two archetypal profile shapes: a block-shaped profile where the concentration of aerosols and trace-gases is constant up to a certain height, and a profile where these concentrations decrease exponentially with height.

Measurements of aerosol optical thickness (AOT), and retrievals of aerosol single-scattering albedo ($\bar{\omega}$ or SSA) over the Highveld are available from the AERONET sun photometer that was situated at the University of the Witwatersrand in Johannesburg during 2007 and 2009. These measurements are summarised in Table 1. The intention is not a detailed analysis of the AERONET record, but rather to determine reasonable AOT and $\bar{\omega}$ magnitudes for input into the radiative transfer model.

Unlike the study of Leitão et al. (2010), wherein vertical profiles representative of urban and rural scenes with different VCD and AOT values were used, the present idealized scenarios are designed in the light of the values shown in Table 1 to all have the same AOT of 0.3, and the same NO_2 VCD of $20\,\mathrm{petamolec\,cm^{-2}}$ ($2\times10^{16}\,\mathrm{molec\,cm^{-2}}$). The NO_2 volume mixing ratio (VMR) between the top of the block, and either the elevated layer above, or the top of the model grid is set at 1.0×10^{-11} (10ppt), in order to avoid undefined block-AMFs in these parts of the vertical grid (a block-AMF is similar to an AMF, but for a subset of the total vertical column). Scenarios are introduced where an elevated layer of aerosols and trace gases are added to the profile shape, as has been observed during this and other field campaigns in the region. Since large portions of the Highveld are at altitude, the

Table 1. A summary of AERONET sun photometer measurements of aerosol optical thickness (AOT) and single-scattering albedo (SSA) at the University of the Witwatersrand in Johannesburg during late winter 2007 and 2009. Only one SSA retrieval was made during September 2007 hence no minimum and maximum values are shown.

		AOT		SSA	
		2007	2009	2007	2009
July	Min	0.03	0.01	0.60	0.78
	Mean	0.13	0.11	0.80	0.83
	Max	0.47	0.45	0.94	0.87
August	Min	0.06	0.01	0.78	0.80
	Mean	0.20	0.17	0.82	0.91
	Max	0.62	0.57	0.87	0.95
Sept	Min	0.11	0.21		0.85
	Mean	0.27	0.33	0.88	0.87
	Max	0.42	0.39		0.94

effect of a change in surface elevation from sea-level to 1400m above sea-level is evaluated. The twelve model scenarios' profile shapes are shown in Fig. 4.

The radiative transfer model (RTM) is run at a wavelength of 440nm, with the surface albedo set at 0.02, 0.05, 0.08 and 0.11. The solar zenith angle is varied from 25°–60° in steps of 5°. Aerosols are modelled using single-scattering albedos ($\bar{\omega}$) of 0.82, 0.90 and 0.98; and a Henyey-Greenstein asymmetry parameter of 0.7 (Henyey and Greenstein, 1941). An altitude grid of 200m-thick layers from the surface up to 10000m is used. The aircraft altitude is fixed at 6000m above sea level in all scenarios. Lambertian surface reflectance is assumed.

Calculated AMFs are summarised in Fig. 5: at the two surface elevations modelled (i.e. 0m and 1400m), AMFs appear to be constrained between a minimum- and maximum-AMF surface. For a given combination of altitude, SZA and surface albedo, variation in the AMF is due to variation in the profile shape and aerosol single-scattering albedo. Although these scenarios are by no means exhaustive, they are representative of what is frequently found in the atmosphere above the Highveld, and allow the uncertainty in the AMF to be constrained.

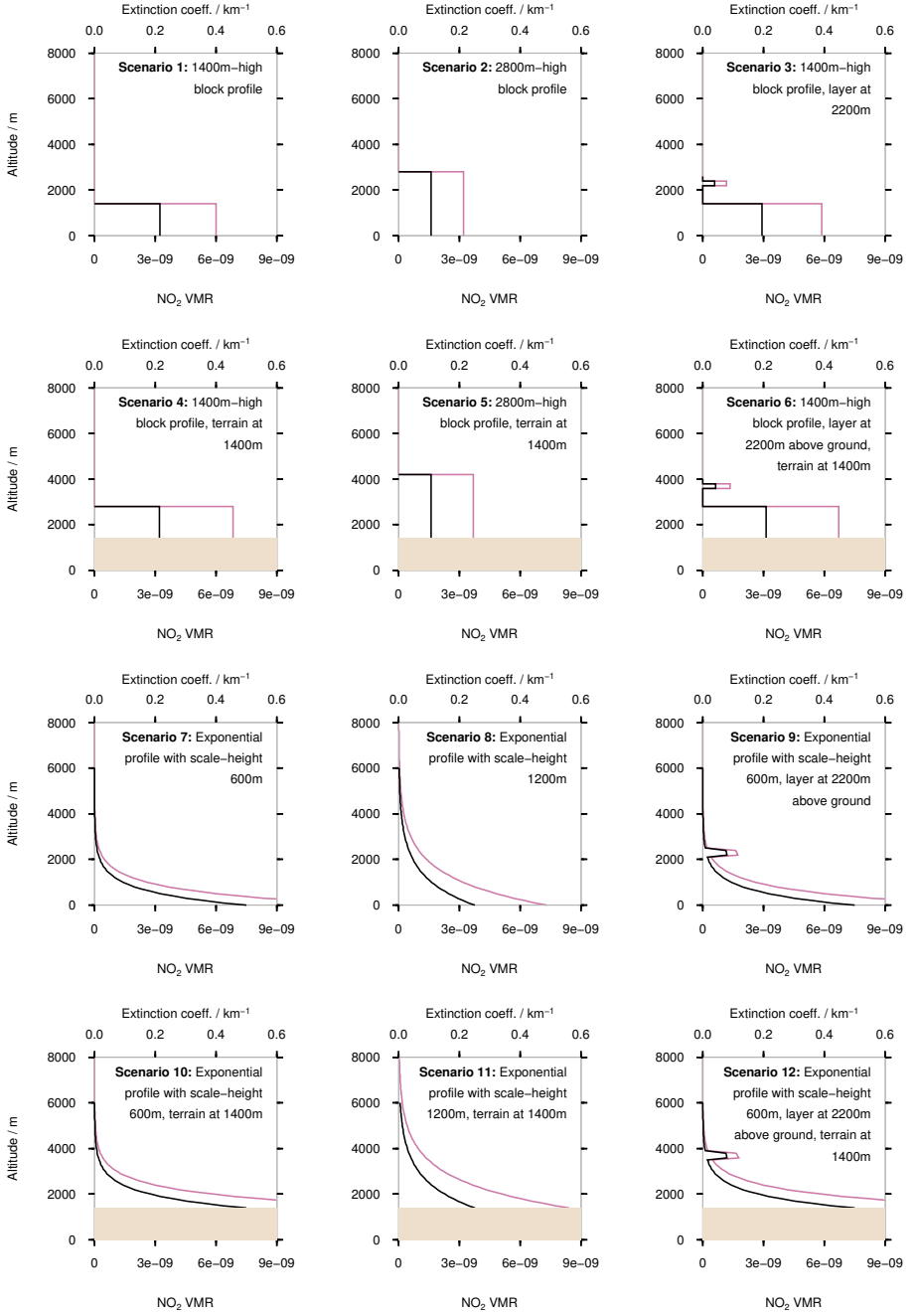

Figure 4. Profile shapes of aerosol extinction coefficient (black line) and NO_2 mixing ratio (purple line) for the twelve scenarios used in the radiative transfer model sensitivity study. The scenarios are designed to all have the same AOT and NO_2 VCD. Terrain height is indicated by the shaded light-brown area. Note that the vertical grid used in the model extends up to 10000m

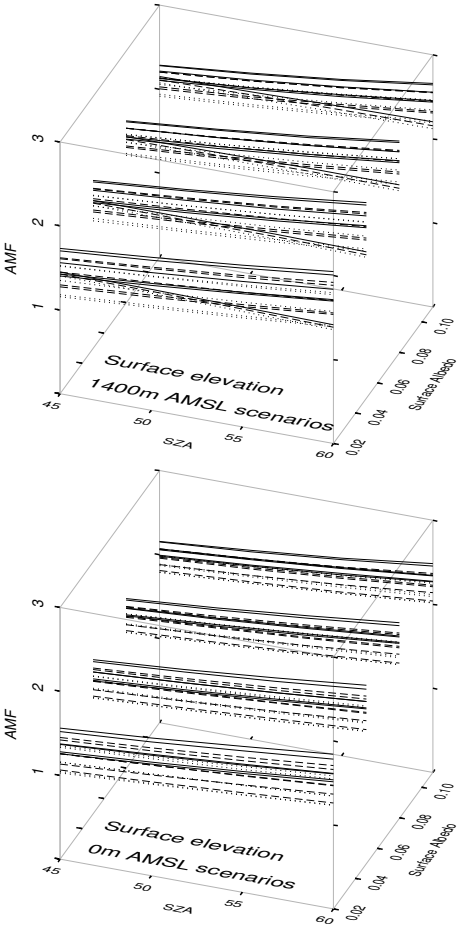

Figure 5. Calculated air-mass factors from the twelve scenarios outlined in Fig. 4, plotted as a funcion of solar zenith angle and surface albedo for the high-surface-elevation scenarios (top) and sea-level scenarios. A dotted line indicates $\bar{\omega}$=0.82, a dashed line $\bar{\omega}$=0.90 and a solid line $\bar{\omega}$=0.98. In general, an increase in AMF with increasing single-scattering albedo is found. Variation in the AMF due to variations in aerosol properties and vertical profile shape are bounded by a minimum- and maximum-AMF surface at each surface elevation.

5 Airborne DOAS measurements

The high spatial resolution (around 80m) aircraft measurements from the iDOAS (Heue et al., 2008), when combined with a flight path following the satellite track, might be thought of as giving a transect of each satellite ground pixel. Two approaches are taken in order to make a comparison between measurements from the two platforms: a time-domain moving-average of the aircraft VCD measurement and a spatial average of the high-resolution aircraft measurements within each satellite pixel.

Variability in the AMF for the aircraft measurements is constrained between the minimum- and maximum AMF surfaces described above in relation to Fig. 5. In order to determine the maximum- and minimum AMF, and hence the uncertainty in the VCD due to the aerosol profile shape in the vertical column density, successive linear interpolations between data points along SZA, surface albedo, and surface-elevation axes are performed for each iDOAS measurement. Solar zenith angle is calculated from the aircraft time and position using the pyEphem package (Rhodes, 2015). Surface albedos are sampled from the OMI albedo climatology (Kleipool et al., 2008), hence the spatial resolution of the albedo map is limited to half a degree. Surface elevation is sampled from the US Geological Survey GTOPO-30 global digital elevation model with spatial resolution of approxiamately 1km.

Aircraft SCDs are shifted using an offset to bring background aircraft VCD values in line with satellite tropospheric vertical column densities (TVCD), based on the assumption that the satellite instrument's background measurements over remote ocean areas better approximate a zero-NO_2-column measurement. For the flight maps presented below, the mean of the minimum- and maximum AMF was used to calculate the VCD; for the time-series plots the mean AMF is used, with error-bars defined by the VCD's calculated using the minimum- and maximum AMF.

In general cloud-free conditions were encountered during all of the flights. The exception to this is the flight on 11 August, where approximately one octa of thin cirrus cloud cover was observed above the aircraft, estimated to be at around 10000m. Based on the radiative-transfer-modelling study of Kokhanovsky and Rozanov (2009), the TVCD error caused by clouds in the OMI measurement is estimated to be less than -10%. The effect of such clouds on errors in the aircraft measurement is not quantified, however it is likely to be less than this.

Figure 6 shows a map of tropospheric vertical column density (TVCD) from the Derivation of OMI tropospheric NO2 (DOMINO) V2.0 product for 9 August 2007, with the flight track and NO_2 VCD from the airborne instrument overlaid. Hourly-average wind directions from several weather stations are shown for the hour of the aircraft's overpass and the previous two hours. A time-series comparison of the airborne DOAS nadir NO_2 VCD with OMI TVCD on this day is shown in Fig. 7. In the time-series plot, airborne DOAS measurements are shown with error-bars representing the uncertainty in the AMF, along with the OMI pixel at aircraft nadir (orange) as well as one OMI-row to the west (blue) and east (yellow) of the aircraft. Spatially-averaged full-resolution iDOAS

measurements within the OMI pixel at aircraft nadir are shown in grey, with one standard deviation in measured variability above and below the average shown by error-bars. The first subsidiary plot in Fig. 7 shows the surface elevation (grey) and surface albedo (orange) at aircraft nadir; the second subsidiary plot shows solar zenith angle at the aircraft's time and position (orange) as well as the minimum (grey) and maximum (cyan) AMF derived using the interpolation procedure described above. Aircraft time is indicated on the lower horizontal axis; the corresponding distance along the aircraft track is shown on the upper horizontal axis. Plots for subsequent flights present the measurements in a similar fashion.

Figure 8 shows the airborne full-resolution iDOAS measurements for all the flights, averaged within the satellite pixel at aircraft nadir, compared with the NO_2 TVCD satellite product in that pixel. Error bars once again indicate one standard deviation in measured variability above and below the average. The figure inset shows a magnified view of the values lower than $7\,\mathrm{petamolec\,cm^{-2}}$. The regression lines plotted in the inset are fitted through value pairs with satellite TVCD less than $5\,\mathrm{petamolec\,cm^{-2}}$; the regression lines in the main figure are fitted through value pairs with satellite TVCD greater than this.

Between 12:25 and 12:40 UTC on 9 August (Fig. 7) the aircraft measured background values of NO_2 VCD: less than $5\,\mathrm{petamolec\,cm^{-2}}$. Examining Fig. 8, for this particular flight the slope of the fitted straight line is 0.38 for low VCDs, indicating, notwithstanding a low regression coefficient, that the OMI measurements observe a steeper gradient than the iDOAS for background values of NO_2 VCD.

The airborne iDOAS measurements on this day also included industrial plumes and urban areas. Weather-station data from Grootvlei indicates an hourly-average wind direction of 219° and $3.11\,\mathrm{m\,s^{-1}}$ for 12:00–13:00 UTC. The aircraft track is between 36km–48km downwind, and we might naïvely estimate that the plume is between approximately 3h – 4h old when it was measured by the iDOAS.

Between 12:45 and 12:46, a small peak in the airborne DOAS VCD of $8.1\pm1.3\,\mathrm{petamolec\,cm^{-2}}$ is observed. The OMI product and the spatially-averaged iDOAS within the OMI pixel are in good agreement (both $11\,\mathrm{petamolec\,cm^{-2}}$); however since the spatial extent of the OMI pixel includes the gradient forming the larger plume described below, the iDOAS measures variation across this pixel of almost half an order of magnitude, from 5.2–$21.1\,\mathrm{petamolec\,cm^{-2}}$. At this position, the upwind OMI pixel has a TVCD of $34\,\mathrm{petamolec\,cm^{-2}}$, which is closer to the magnitude of the peak measured by the iDOAS in the following (i.e. later in time and further along the aircraft flight direction) OMI pixel.

This peak is on a spatial scale of an OMI pixel, with maximum iDOAS VCD of $34\pm5.5\,\mathrm{petamolec\,cm^{-2}}$ at 12:48 UTC. At this position OMI TVCD is $15\,\mathrm{petamolec\,cm^{-2}}$, however the upwind OMI pixel, which since the aircraft is at the upwind edge of the pixel at nadir, is perhaps more representative of what the aircraft measured, is $24\,\mathrm{petamolec\,cm^{-2}}$. Spatially-averaged iDOAS VCD within this

OMI pixel is 29 $\mathrm{petamolec\,cm^{-2}}$, 93% greater than the nadir OMI pixel and 21% greater than the upwind pixel. Examining the satellite and aircraft times in Fig. 6, we see that the iDOAS measured this plume approximately fourty minutes later than OMI. During this time it is possible that the position of the plume moved, making a comparison of the iDOAS with the previous upwind OMI pixel (i.e. where the plume was when OMI measured it) relevant. In this case we find that the OMI $\mathrm{NO_2}$ TVCD of 34 $\mathrm{petamolec\,cm^{-2}}$ is 17% higher than the spatially-averaged iDOAS, and approximately the same as the peak iDOAS VCD.

Between the Vaal Triangle and the city of Johannesburg, a decrease in $\mathrm{NO_2}$ VCD is found in both the aircraft and satellite measurements. In this area, horizontal $\mathrm{NO_2}$ gradients are shallower, and variability within each OMI pixel is smaller. However, the OMI product is about 20% lower than the spatially-averaged iDOAS. From about 12:52 the iDOAS started to measure the steep horizontal gradient found over the urban areas to the east of Johannesburg.

Approaching the industrialised eastern part of Johannesburg and passing overhead O.R. Tambo International Airport a increase in the $\mathrm{NO_2}$ VCD of 77 $\mathrm{petamolec\,cm^{-2}}$ over a distance of approximately 50km was found, with the $\mathrm{NO_2}$ VCD peaking at 95$\pm$15 $\mathrm{petamolec\,cm^{-2}}$ The spatial scale of the roll-off of this peak towards the north is similar to the increase on the southern side. The OMI product at this position gives a much lower $\mathrm{NO_2}$ VCD of around 25 $\mathrm{petamolec\,cm^{-2}}$. The spatially-average iDOAS measurements within this OMI pixel is 140% greater at 60 $\mathrm{petamolec\,cm^{-2}}$. The upwind OMI pixel is around 27 $\mathrm{petamolec\,cm^{-2}}$, downwind is 13 $\mathrm{petamolec\,cm^{-2}}$, however $\mathrm{NO_2}$ gradients do not necessarily align themselves conveniently with the flight track of research aircraft or satellites, and given that the source of the plume is the urban areas within the city, the gradient in the across-track direction is likely to be as steep as that in the along-track direction. The imaging swath of the airborne DOAS is around 1980m from 4500m above the ground, which is too narrow to make observations on the spatial scale of a satellite pixel; in the case of OMI, 24km wide. Within the following OMI pixel the spatially averaged iDOAS (48 $\mathrm{petamolec\,cm^{-2}}$) is 65% greater than the OMI product (29 $\mathrm{petamolec\,cm^{-2}}$) In Fig. 8, a regression line is fitted through OMI-pixel-averaged aircraft data compared with the OMI $\mathrm{NO_2}$ product, for values greater than 5 $\mathrm{petamolec\,cm^{-2}}$. The slope of this line is 2.4, indicating that for the young industrial plumes and urban areas measured during this flight, OMI substantially underestimates $\mathrm{NO_2}$ VCD.

Some smaller peaks in the $\mathrm{NO_2}$ VCD of around 10 $\mathrm{petamolec\,cm^{-2}}$ measured west of Pretoria by the iDOAS around 13:00 UTC are observed with OMI's resolution to be a broad area of $\mathrm{NO_2}$ VCD around 16 $\mathrm{petamolec\,cm^{-2}}$ at aircraft nadir. Further north along the flight track, $\mathrm{NO_2}$ VCDs measured by the iDOAS and OMI gradually decrease to background values where once again a reasonably good match is found between the two instruments.

On 11 August (shown in Fig. 9 and 10 as a map and time-series respectively), with the exception of a small plume that was measured by the aircraft around 12:05 UTC, a reasonable agreement is found between the airborne iDOAS measurement and OMI product while measuring the gradual in-

crease in NO_2 VCD between 11:40 at Richards Bay and 12:10 at the southern border of Swaziland. Referring to Fig. 8, the regression line for low VCDs shown in the inset has a slope of 0.55, indicating that the satellite measurements will show steeper gradients than the aircraft measurements, however this slope is closer to unity than for the other flights. Wind measurements at Camden on the eastern Highveld of $8.6\mathrm{m\,s^{-1}}$ for 14:00 local time allow a naïve estimate of plume age from approximately $5\mathrm{h}$ for the closest power station (approximately $145\mathrm{km}$ as the wind blows) to $12\mathrm{h}$ for the Vaal Triangle and the city of Johannesburg, approximately $360\mathrm{km}$ away. In reality, the plumes are probably older than this, since the wind speeds in the $12\mathrm{h}$ prior to the flight were lower. This is slightly older than the Vaal Triangle plume measured on 9 August, and clearly much older than the NO_2 plume measured overhead the city of Johannesburg on that day, which is measured at the source.

The small plume encountered at 12:05 is likely from a forest fire, of which many were observed from the aircraft on this day. Following this, around 12:14 the plume appearing to originate from the Vaal Triangle and the most southern of the power stations was measured by the iDOAS. In this case, OMI NO_2 VCD of 12 $\mathrm{petamolec\,cm^{-2}}$ is higher than both the peak (9.8 $\mathrm{petamolec\,cm^{-2}}$) and the spatially-averaged iDOAS measurement (8.9 $\mathrm{petamolec\,cm^{-2}}$). The upwind OMI pixel is slightly lower than the aircraft-nadir pixel, the downwind pixel is substantially higher at 18 $\mathrm{petamolec\,cm^{-2}}$, but in this case the plume had started to merge with the larger northern plume from the Highveld. Measured variation across these OMI pixels is small, for example the standard deviation for the OMI pixel centred at 12:13 aircraft time is 1.3 $\mathrm{petamolec\,cm^{-2}}$, compared to the average of the iDOAS measurements at 8.9 $\mathrm{petamolec\,cm^{-2}}$, the standard deviation is 14% of the mean.

The large northern plume from the Highveld was then measured by the aircraft. This plume has two locii: around 12:25 and 12:32. The peak iDOAS NO_2 VCD in the first locus is 43 ± 6.2 $\mathrm{petamolec\,cm^{-2}}$. Broadly speaking this peak is split across two OMI pixels with approximately the same VCD of 37 $\mathrm{petamolec\,cm^{-2}}$. The spatially-averaged iDOAS measurements in these OMI pixels is close to the OMI measurement: 37 and 36 $\mathrm{petamolec\,cm^{-2}}$. The shoulder of this peak is also well captured by the satellite. Spatially-averaged iDOAS measurements are close to the values measured by OMI. Variation across each of these OMI pixels is larger than in the southern plume with standard deviations 3.9 and 2.4 $\mathrm{petamolec.cm^{-2}}$.

In the second plume locus, the iDOAS peak is a little higher: 47 ± 7.9 $\mathrm{petamolec\,cm^{-2}}$. At this point the OMI measurement is much lower at 28 $\mathrm{petamolec.cm^{-2}}$ and in general it appears that OMI did not measure the same plume shape as the iDOAS. This is possibly because the satellite overpass was $35\mathrm{min}$ earlier than the aircraft, which would give time for the plume locus to shift, although weather stations indicate consitent wind directions during the two hours prior to the aircraft overpass. It is also possible that the very high peak around 12:30 originates from a plethora of local, transient sources in the form of forest-fires, measured by the iDOAS but not by OMI. Some idea of the magnitude of a forest-fire source can be gleaned from inspection the pixels above Nelspruit

around 12:41 aircraft time, which are excluded from Fig. 10 because the aircraft was in a spiral descent at the time and hence the iDOAS measurements are difficult to interpret. In addition, the extreme aerosol loading (shown in the vertical profile measurement shown in Fig. 3) in the forest-fire plumes causes the local AMF to be well outside the scope of the modelled scenarios, leading to an incorrect calculation of the VCD.

In general the reason for the dual locus is not clear; it is perhaps related to the topography where this plume appears to be on either side of a ridge. These two plume locii are resolved by the OMI satellite at aircraft nadir and one line upwind; one line downwind the two plume locii appear to have merged into one. The NO_2 gradient in the roll-off of the peak in the iDOAS measurements appears visually to have the same magnitude as on the southern side, however the measured variability, expressed as a standard deviation is much larger: 7.8 $\mathrm{petamolec\,cm^{-2}}$; expressed as a percentage of the mean this is 41% and this indicates that there is a certain amount of chance involved in the variability within the OMI pixel. On the southern side of this plume the gradient is split across two OMI pixels and hence the variabilty within each pixel is much lower.

The structure seen in the satellite image in Fig. 9 of a southern plume advecting from the Vaal Triangle, and a northern plume from Johannesburg and the cluster of power stations on the eastern Highveld is seen frequently while browsing through the OMI record. In Fig. 8 the regression line in the main figure has a slope of 1.1, indicating that OMI is better able to capture the shallower NO_2 VCD gradients in an aged plume better than in the young plumes and urban areas measured on 9 August.

The flight on 18 August routed close to the power stations on the Eastern Highveld. The first plume can be identified in Fig. 11 and 12 from the airborne iDOAS measurements between 12:35 and 12:50 UTC. From the OMI image it would appear that this plume is a composite of the aged plume from the Vaal Triangle, and younger plumes from Tutuka and Majuba power stations as well as Secunda. The aircraft track was approximately 55km downwind of Majuba, 110km downwind of Tutuka power station and 140km downwind of Secunda. The Vaal Triangle was approximately 250km upwind of the aircraft. Weather station measurements from nearby Tutuka indicate windspeeds of 2.1$\mathrm{m\,s^{-1}}$, giving a naïve estimate of plume age ranging from 7h from Majuba to 18h from Secunda.

An initial small peak NO_2 VCD of 26$\pm$4.5 $\mathrm{petamolec\,cm^{-2}}$ around 12:41 aircraft time appears to be from a dispersed plume originating from Tutuka and Majuba power stations, and Secunda. NO_2 measured by OMI at aircraft nadir is 15 $\mathrm{petamolec\,cm^{-2}}$; the VCDs in the upwind and downwind pixels are both lower. The spatially-averaged iDOAS measurement is 66% greater at 25 $\mathrm{petamolec\,cm^{-2}}$ within this OMI pixel. The steep NO_2 gradient leading up to this peak is split across two OMI pixels, hence the measured variability within each pixel is low. In contrast the gradient in the NO_2 VCD leading to the next peak around 12:45 aircraft time is contained within one OMI pixel. The spatially-averaged iDOAS in this pixel is 32 $\mathrm{petamolec\,cm^{-2}}$, with the standard

deviation of the measured variability at 7.3 $\mathrm{petamolec\,cm^{-2}}$, which is 23% of the average. The OMI measurement is 45% lower at 22 $\mathrm{petamolec\,cm^{-2}}$.

The peak NO_2 VCD measured by the aircraft around 12:45 is $58\pm10\,\mathrm{petamolec.cm^{-2}}$. At this position, the OMI pixel at aircraft nadir is 22 $\mathrm{petamolec\,cm^{-2}}$ less than half of the peak measured by the airborne iDOAS; the upwind pixel slightly higher than the aircraft-nadir OMI pixel at 32 $\mathrm{petamolec\,cm^{-2}}$. The spatially-averaged iDOAS measurement in the nadir OMI pixel is 47 $\mathrm{petamolec\,cm^{-2}}$, 113% greater than the OMI measurement. Although the structure of this plume can be seen in the OMI image, the VCD magnitudes measured are substantially smaller than those measured by the airborne DOAS.

The aircraft crosses a plume from Matla and Kriel power stations around 12:55 with peak NO_2 VCD of $65\pm11\,\mathrm{petamolec\,cm^{-2}}$. This measurement is around 125km downwind and a naïve estimate of the plume age is approximately 12h. Again, the structure of the plume is observed by OMI, but the magnitudes of the vertical column densities are lower by almost half compared to those measured by the aircraft. Variability across the OMI pixel containing the major NO_2 gradient is 5.8 $\mathrm{petamolec\,cm^{-2}}$ expressed as a standard deviation. The spatially-averaged iDOAS measurement within the nadir OMI pixel is 57 $\mathrm{petamolec\,cm^{-2}}$. In contrast, the OMI measurement is 39 $\mathrm{petamolec\,cm^{-2}}$, 32% lower.

A third plume is measured by the aircraft between 13:00 and 13:05, this time between 15km – 50km downwind of industrial sources, with two peaks: 83 $\mathrm{petamolec\,cm^{-2}}$ at 13:01 which would appear to originate from Komati power station, and another with peak NO_2 VCD of 63 $\mathrm{petamolec\,cm^{-2}}$ perhaps originating from Duvha power station. Plume age estimates are approximately 4h in both cases with the aircraft measurement 30km downwind. In the case of the plume at 13:01, the aircraft-nadir OMI measurement of 40 $\mathrm{petamolec\,cm^{-2}}$ is less than half of the peak aircraft measurement. The spatially-averaged iDOAS measurement in this OMI pixel is 69 $\mathrm{petamolec\,cm^{-2}}$, which is 73% higher than OMI.

The aircraft measurement resolves a shoulder on the northern side of the first peak, which could be the plume originating from Hendrina power station. The broad structure of these two peaks is observed by OMI, however the measured NO_2 VCD is substantially lower, peaking at 44 $\mathrm{petamolec\,cm^{-2}}$. In contrast, the spatially-averaged iDOAS measurement is 57 $\mathrm{petamolec\,cm^{-2}}$, 30% higher.

The regression through OMI-pixel-averaged aircraft measurements compared with the OMI product from 18 August in Fig. 8 has a slope of 1.5. This reflects the lower NO_2 VCDs measured by OMI in comparison to the iDOAS, described above in relation to the time-series in Fig. 12. Comparing the three flights that were performed to track the AURA satellite, we find a relation between the slope of the regression line and the distance of the measurement from the source. For the flight on 9 August, which passed approximately 40km downwind of the Vaal Triangle and directly overhead Johannesburg the slope of the regression line is 2.4. Measurements on 11 August, between 145 – 360km downwind of sources give a slope of 1.1 and the measurements on 18 August, where the

aircraft was 55 – 150km downwind of major sources gives an intermediate slope of 1.5. Plume dispersion occurs by turbulent mixing in the boundary layer, which is related to surface topography and instability (i.e. thermals). Both of these are spatial features of the landscape hence the relationship with distance downwind, rather than the time taken to travel the distance.

It is clear from inspection of the iDOAS measurements in Fig. 9 that our approach of using a range of AMFs to calculate the VCD results in a variability in the VCD that scales with SCD. This is simply a mathematical effect that is obvious from Eq. 2. It is interesting to note in the OMI measurements that the downwind pixels (yellow) reproduce the plume structures observed in the aircraft-nadir OMI pixels (bold orange), with a consistently lower VCD. This would indicate a steady decrease in the amount of $\mathrm{NO_2}$ in the air, probably due to chemical conversion into another species. $\mathrm{NO_2}$ emitted from industries in the Vaal Triangle is also visible in the satellite measurements shown in Fig. 11; likewise for the city of Johannesburg.

A comparison between the airborne iDOAS and SCIAMACHY can be made from the flight on 14 August. In this case it would appear that SCIAMACHY resolves a steeper gradient than the airborne instrument. This unexpected result can be partly exlained as a spatial artifact: the satellite pixel between 08:10 and 08:14 aircraft time in Fig. 14 would be affected by the plume that would appear to be from Majuba power station (see Fig. 13), measured at around 08:08 by the aircraft. The mismatch between the SCIAMACHY pixel further South along the aircraft flight track and the measurement made by the aircraft between 08:15 and 08:19 is more difficult to explain. Comparing the performance of OMI and SCIAMACHY against the iDOAS, one would expect OMI, given its higher spatial resolution, to be better able to capture the peak VCD's in the narrow plumes found on the Highveld. It appears that this is not the case, however the reason for this is not clear; perhaps it is related to the different instantaneous fields of view of the two instruments.

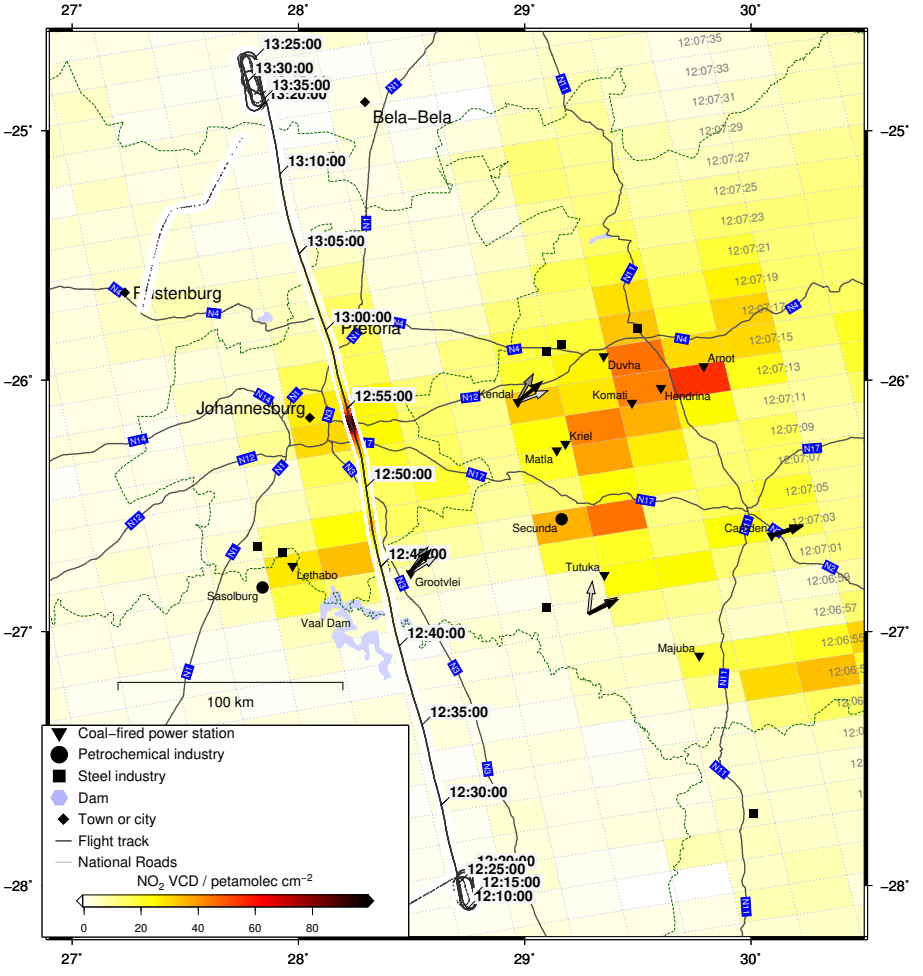

Figure 6. A comparison of the airborne DOAS NO_2 vertical column densities (indicated by colour along the flight track) with OMI DOMINO V2.0 (coloured rectangles) on 9 August 2007. UTC aircraft time is indicated every five minutes along the flight track (black line running from approximately 28°S, 28.8°E to 24.8°S, 27.8°E). UTC satellite time is shown for each row. Hourly-average wind directions for several weather stations are shown for the hours up to 13:00 UTC (black arrow), 12:00 UTC (dark grey arrow) and 11:00 UTC (light grey arrow).

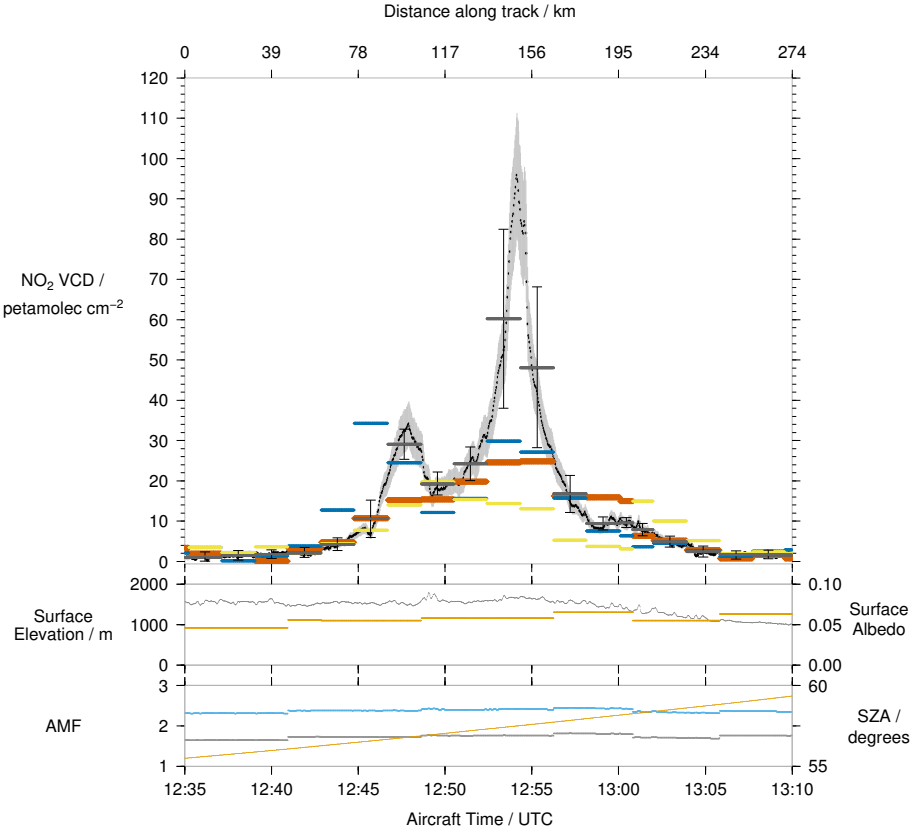

Figure 7. A timeseries of the airborne DOAS NO_2 vertical column densities on 9 August 2007, DOMINO V2.0 at aircraft nadir (orange) and one OMI line west (blue) and east (yellow) of aircraft nadir. Aircraft measurements averaged over the area of each OMI pixel are shown in grey, with one standard deviation in measured variability above and below the average indicated with error-bars. Surface elevation and surface albedo are shown in the first sub-plot. The second sub-plot shows the minimum and maximum AMF estimates (grey and blue), and the solar zenith angle (orange) at aircraft time and position.

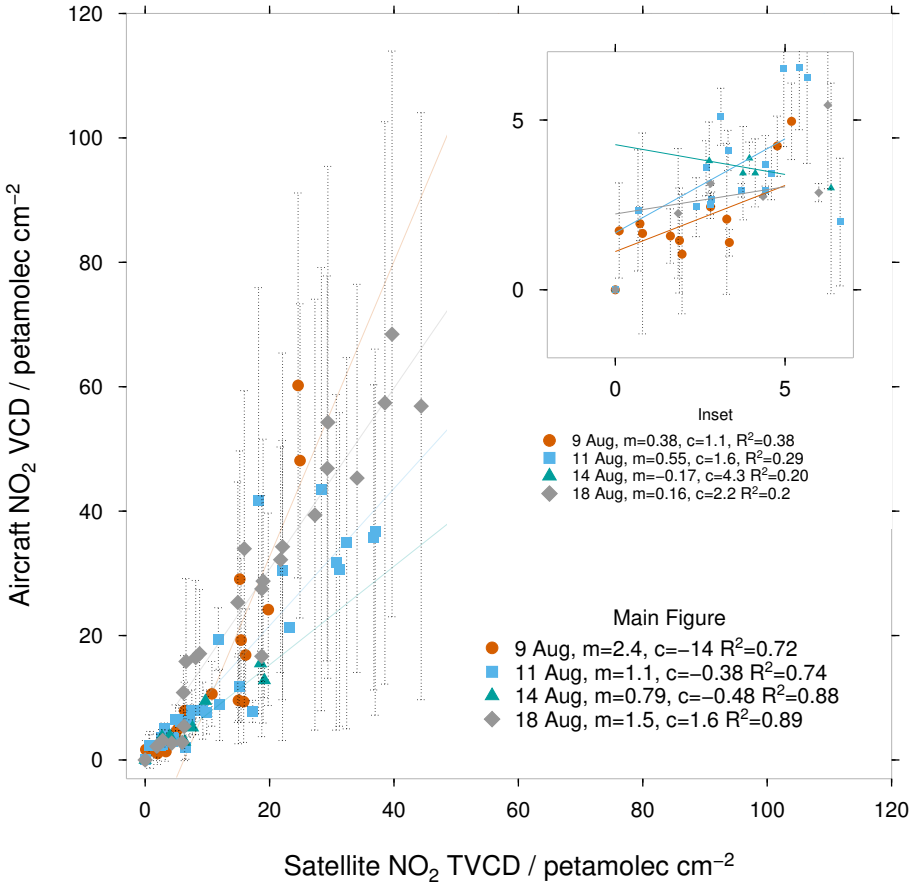

Figure 8. OMI and SCIAMACHY measurements compared with co-located spatially-averaged aircraft measurements. Aircraft iDOAS VCD is calculated using the mean of the minimum- and maximum-AMF calculated for the high-resolution measurement. Error-bars indicate the minimum- and maximum iDOAS VCD found within the satellite pixel. In the inset figure, a linear regression line is fitted through all background measurements less than 5 $\mathrm{petamolec\,cm^{-2}}$. In the main figure, the regression lines are fitted through measurements greater than 5 $\mathrm{petamolec\,cm^{-2}}$ for each flight. The slope (m) of the regression line for each day is indicated, as well as the y-intercept (c) and the regression coefficient (R^2).

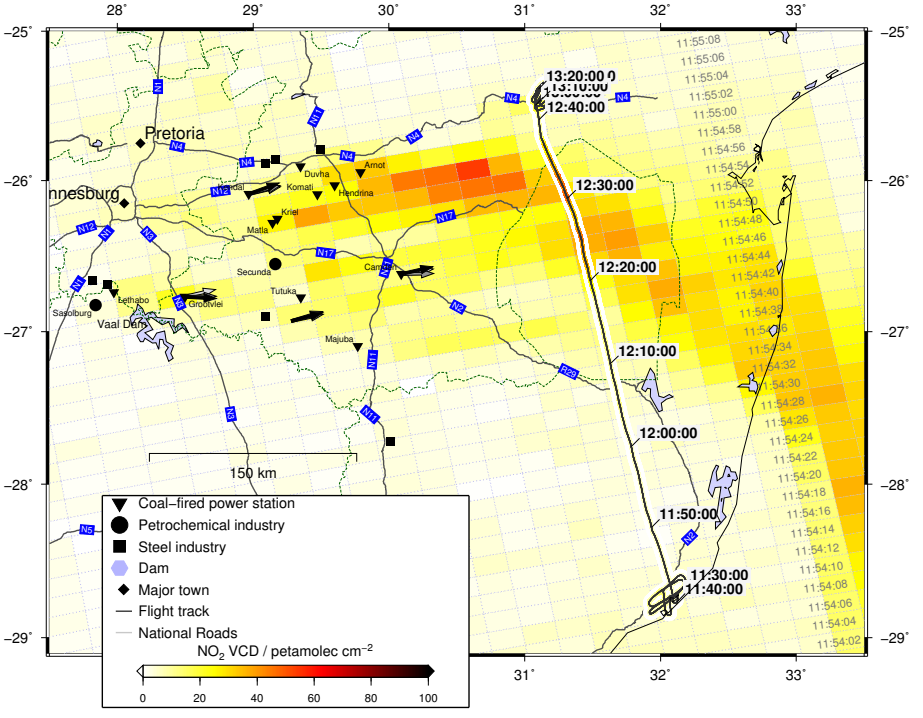

Figure 9. A comparison of the airborne DOAS NO_2 vertical column densities between Richards Bay and Nelspruit with OMI DOMINO V2.0 on 11 August 2007. Data presentation is as in Fig. 6.

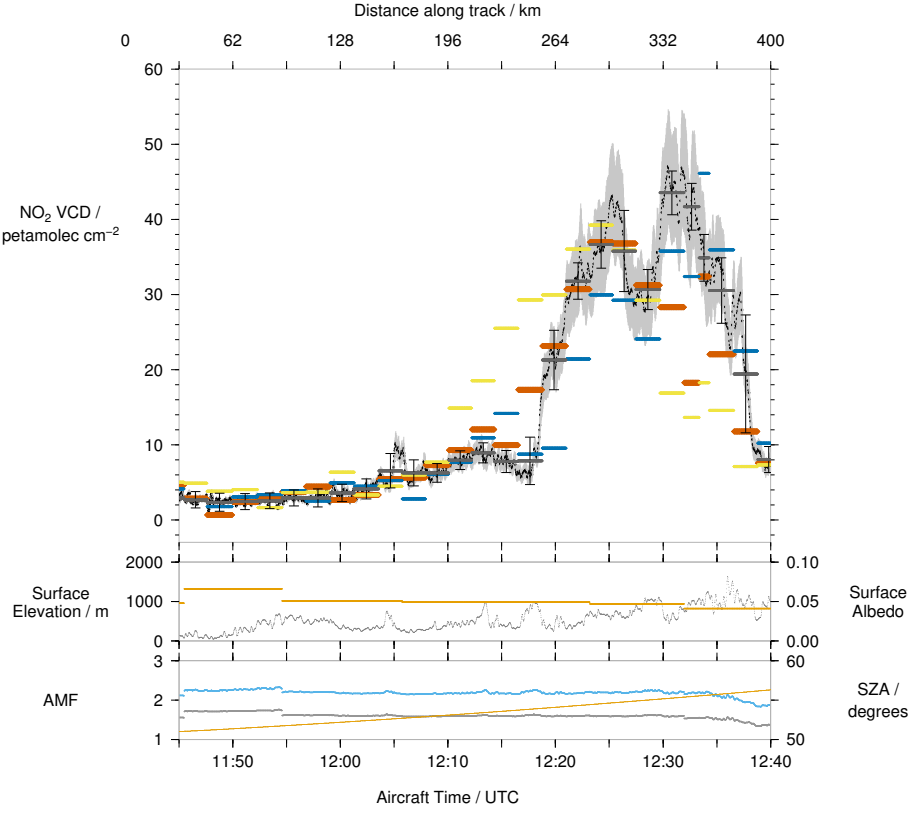

Figure 10. A timeseries of the airborne DOAS NO_2 vertical column densities on 11 August 2007, DOMINO V2.0 at aircraft nadir (orange) and one OMI line west (blue) and east (yellow). Aircraft measurements averaged over the area of each OMI pixel are shown in grey. Sub-plots are as described for Fig. 7.

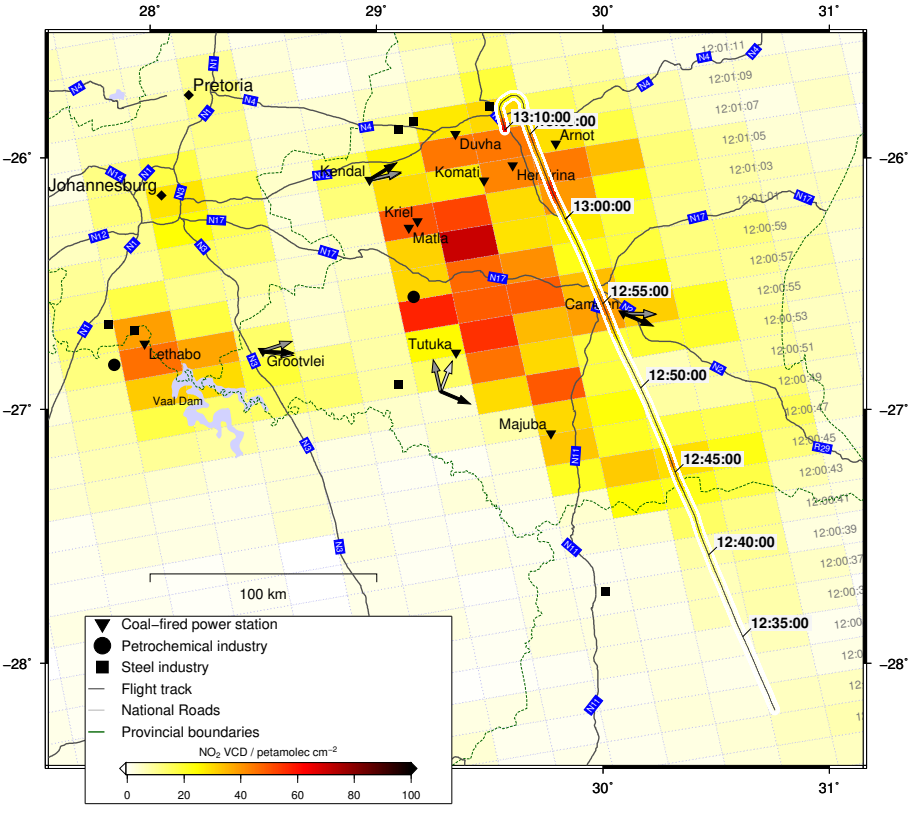

Figure 11. A comparison of the airborne DOAS NO_2 vertical column densities with DOMINO V2.0 on 18 August 2007. Data presentation is as in Fig. 6

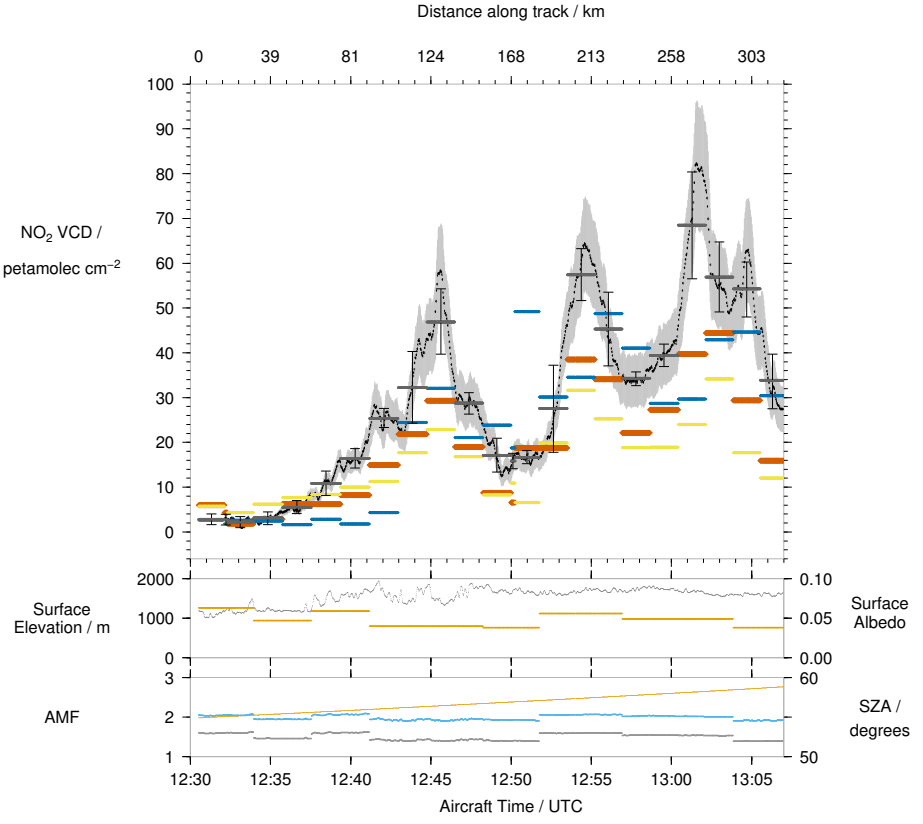

Figure 12. A timeseries of the airborne DOAS NO_2 vertical column densities on 18 August 2007, DOMINO V2.0 at aircraft nadir (orange) and one OMI line west (blue) and east (yellow). Aircraft measurements averaged over the area of each OMI pixel are shown in grey. Sub-plots are as described for Fig. 7

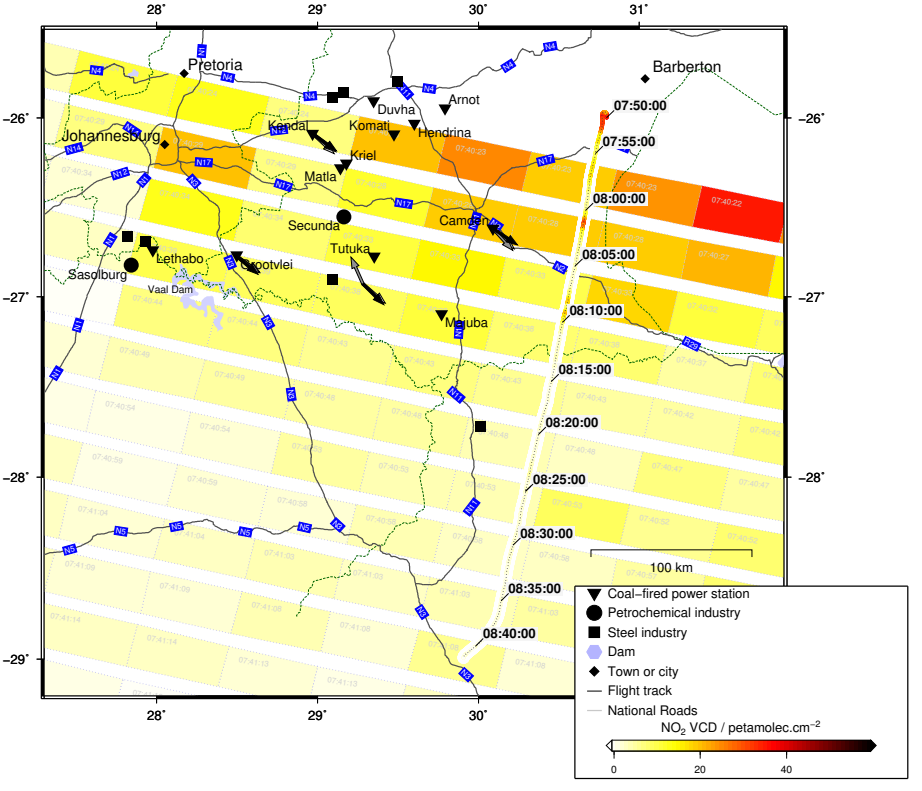

Figure 13. A comparison of the airborne DOAS NO_2 vertical column densities with SCIAMACHY on 14 August 2007. Data presentation is as in Fig. 6, however since SCIAMACHY is a whiskbroom instrument, times for each satellite pixel are shown.

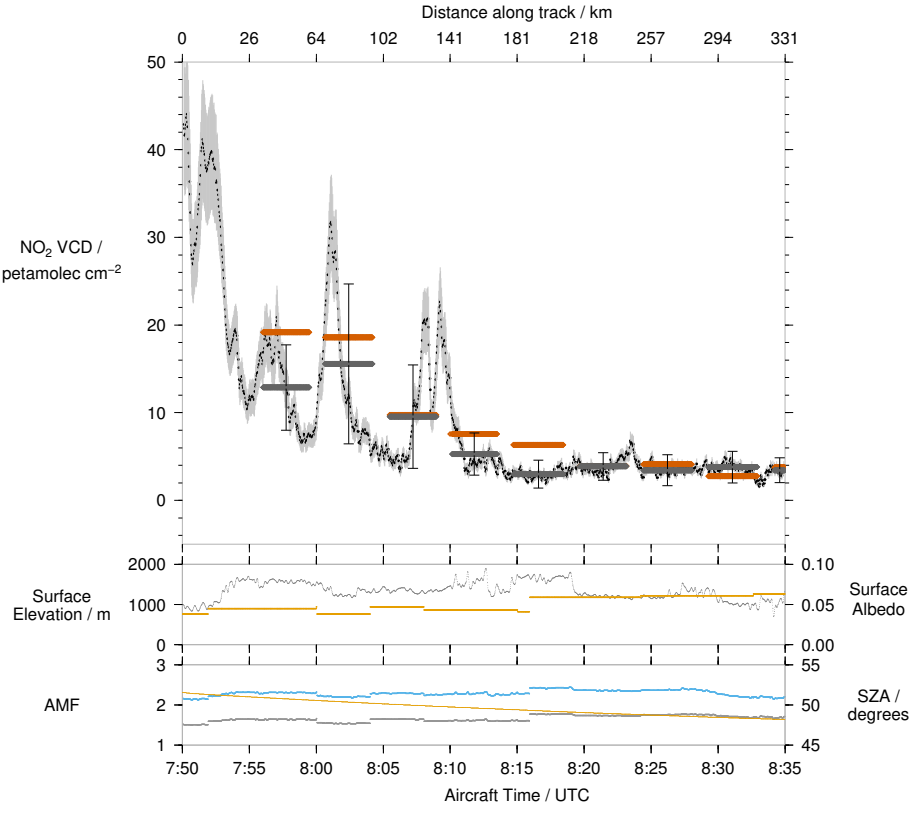

Figure 14. A timeseries of the airborne DOAS NO_2 vertical column densities on 14 August 2007 , SCIAMACHY at aircraft nadir (orange) and OMI DOMINO V2.0 at aircraft nadir (yellow). Aircraft measurements averaged over the area of each OMI pixel are shown in grey. Sub-plots are as described for Fig. 7

6 Conclusions

Four research flights were performed over the Highveld region of South Africa during August 2007 using an airborne imaging DOAS instrument to measure NO_2 column densities, a Particle Measurement Systems PCASP probe to measure aerosol size distribution and number density, and a chemiluminescence in-situ NO_y instrument. These flights were planned to co-incide with overpasses of the OMI and SCIAMACHY satellite instruments. Each flight included a vertical profile measurement at the beginning and end of the airborne DOAS measurement segment.

Vertical profile measurements of NO_y and aerosol particle number concentrations, although compromised by problems with instruments and limitations due to flight safety requirements, reveal several features. Profile shapes can be approximated by a block-shape and an exponentially-decreasing profile of trace-gas and aerosol concentration, and elevated layers of enhanced concentration are frequently present over the Highveld. Observations of aerosol optical thickness and single-scattering albedo from AERONET during July to September 2007 and 2009 are used to determine representative values for these parameters.

These observations are used to devise a number of scenarios, which are used in a sensitivity study using the SCIATRAN radiative transfer model. A minimum- and maximum air-mass factor is found for a given combination of surface elevation and albedo, and solar zenith angle. The difference between the minimum and maximum air-mass factor represents uncertainty due to the profile shape and aerosol properties. These air-mass factor estimates are used to calculate vertical column densities from the slant-column densities measured by the iDOAS instrument . These are then compared to satellite tropospheric NO_2 products from OMI and SCIAMACHY. The present approach to quantification of the uncertainty in the air-mass factor, and hence vertical column density, implies that the uncertainty in the vertical column density scales with the magnitude of the slant column density.

The airborne DOAS instrument's much higher spatial resolution, even when averaged using a moving average on a spatial scale of approximately $1.2\mathrm{km}$, reveals spatial gradients in NO_2 that are much steeper than those observed by the satellites. Large-scale features are resolved by the satellites, however peak NO_2 vertical column densities observed by the aircraft are in some cases more than double the satellite measurement. The performance of the satellite measurement is better for more dispersed plumes.

Close to industrial and urban sources, airborne iDOAS measurements spatially averaged over the scale of a satellite pixel are more than twice as high as the co-located satellite measurement. In general, agreement between spatially-averaged iDOAS NO_2 VCD and the satellite measurement improves as the measurements move downwind from the source. For measurements further than approximately $150\mathrm{km}$ downwind, the agreement between the aircraft and OMI is within the margin of error. This is due to the decrease in horizontal NO_2 gradients from turbulence in the mixed layer, which is dependent on spatial features such as surface topography and the distribution of thermals

during the day. As such the agreement between the spatially-averaged iDOAS NO_2 VCD and the satellite product improves with distance, rather than time, downwind of the source.

Inspection of OMI Level-2 satellite images allow plumes from certain point sources on the Highveld to be identified. In other cases, plumes from areas containing several point sources, or areas of effective area sources such as the city of Johannesburg can be identified. During the winter, these plumes are sufficiently stable that they retain their structure for several hundred kilometers downwind. This leads to a northern- and southern plume being visible on the satellite image, corresponding to sources on the eastern Highveld and the Vaal Triangle.

The high spatial resolution of the airborne instrument reveals spatial features in the NO_2 distribution that are not visible even at the relatively high resolution of the OMI sensor. Upcoming satellite missions such as TROPOMI, which have a higher spatial resolution than OMI promise to reveal small-scale features using daily measurements from space.

Acknowledgements. GTOPO-30 DEM data is available from the U.S. Geological Survey. Funding was received from Eskom SOC Ltd. for this project. Thanks to the South African Weather Service, and aircraft crews for support during field campaigns.

References

Annegarn, H. J., Otter, L., Swap, R. J., and Scholes, R. J.: Southern African's ecosystem in a test-tube, South African Journal of Science, 98, 111–113, 2002.

Balashov, N. V., Thompson, A. M., Piketh, S. J., and Langerman, K. E.: Surface ozone variability and trends over the South African Highveld from 1990 to 2007, Journal of Geophysical Research: Atmospheres, pp. 4323–4342, doi:10.1002/2013JD020555.Received, 2014.

Beirle, S., Boersma, K. F., Platt, U., Lawrence, M. G., and Wagner, T.: Megacity emissions and lifetimes of nitrogen oxides probed from space., Science (New York, N.Y.), 333, 1737–9, doi:10.1126/science.1207824, http://www.ncbi.nlm.nih.gov/pubmed/21940891, 2011.

Boersma, K. F., Eskes, H. J., Dirksen, R. J., van der A, R. J., Veefkind, J. P., Stammes, P., Huijnen, V., Kleipool, Q. L., Sneep, M., Claas, J., Leitão, J., Richter, A., Zhou, Y., and Brunner, D.: An improved tropospheric NO₂ column retrieval algorithm for the Ozone Monitoring Instrument, Atmospheric Measurement Techniques, 4, 1905–1928, doi:10.5194/amt-4-1905-2011, http://www.atmos-meas-tech.net/4/1905/2011/, 2011.

Collett, K. S., Piketh, S. J., and Ross, K. E.: An assessment of the atmospheric nitrogen budget on the South African Highveld, South African Journal of Science, 106, 1–9, doi:10.4102/sajs.v106i5/6.220, http://www.sajs.co.za/index.php/SAJS/article/view/220, 2010.

Dentener, F. J., van Weele, M., Krol, M., Houweling, S., and van Velthoven, P.: Trends and inter-annual variability of methane emissions derived from 1979-1993 global CTM simulations, Atmospheric Chemistry and Physics, 3, 73–88, doi:10.5194/acpd-2-249-2002, {\T1\textless}GotoISI{\T1\textgreater}://000180778400002, 2003.

Gottwald, M., Bovensmann, H., and (Eds): SCIAMACHY, Exploring the Changing Earth's Atmosphere, Springer Dordrecht Heidelberg London New York, doi:10.1007/978-90-481-9896-2, 2006.

Haywood, J. M.: Comparison of aerosol size distributions, radiative properties, and optical depths determined by aircraft observations and Sun photometers during SAFARI 2000, Journal of Geophysical Research, 108, doi:10.1029/2002JD002250, http://www.agu.org/pubs/crossref/2003/2002JD002250.shtml, 2003a.

Haywood, J. M.: The mean physical and optical properties of regional haze dominated by biomass burning aerosol measured from the C-130 aircraft during SAFARI 2000, Journal of Geophysical Research, 108, doi:10.1029/2002JD002226, http://www.agu.org/pubs/crossref/2003/2002JD002226.shtml, 2003b.

Henyey, L. and Greenstein, J.: Diffuse radiation in the galaxy, Astrophysical Journal, 93, 70–83, doi:10.1086/144246, 1941.

Heue, K.-P., Wagner, T., Broccardo, S. P., Walter, D., Piketh, S. J., Ross, K. E., Beirle, S., and Platt, U.: Direct observation of two dimensional trace gas distributions with an airborne Imaging DOAS instrument, Atmospheric Chemistry and Physics, 8, 6707–6717, doi:10.5194/acp-8-6707-2008, http://www.atmos-chem-phys.net/8/6707/2008/, 2008.

Hobbs, P. V.: Clean air slots amid dense atmospheric pollution in southern Africa, Journal of Geophysical Research, 108, 1–8, doi:10.1029/2002JD002156, http://www.agu.org/pubs/crossref/2003/2002JD002156.shtml, 2003.

Holben, B. N., Tanre, D., Smirnov, A., Eck, T. F., Slutsker, I., Abuhassan, N., Newcomb, W. W., Schafer, J. S., Chatenet, B., Lavenu, F., Kaufman, Y. J., Castle, J. V., Setzer, A., Markham, B., Clark, D., Frouin, R.,

Halthore, R., Karneli, A., O'Neill, N. T., Pietras, C., Pinker, R. T., Voss, K., and Zibordi, G.: An emerging ground-based aerosol climatology : Aerosol optical depth from AERONET, Journal of Geophysical Research, 106, 12 067–12 097, 2001.

Kleipool, Q. L., Dobber, M. R., de Haan, J. F., and Levelt, P. F.: Earth surface reflectance climatology from 3 years of OMI data, Journal of Geophysical Research: Atmospheres, 113, 1–22, doi:10.1029/2008JD010290, 2008.

Kokhanovsky, A. A. and Rozanov, V. V.: Retrieval of NO 2 vertical columns under cloudy conditions : A sensitivity study based on SCIATRAN calculations, Atmospheric Research, 93, 695–699, doi:10.1016/j.atmosres.2009.01.022, http://dx.doi.org/10.1016/j.atmosres.2009.01.022, 2009.

Leitão, J., Richter, A., Vrekoussis, M., Kokhanovsky, A., Zhang, Q. J., Beekmann, M., and Burrows, J.: On the improvement of NO2 satellite retrievals – aerosol impact on the airmass factors, Atmospheric Measurement Techniques, 3, 475–493, doi:10.5194/amt-3-475-2010, 2010.

Levelt, P. F., Oord, G. H. J. V. D., Dobber, M. R., Mälkki, A., Visser, H., Vries, J. D., Stammes, P., Lundell, J. O. V., and Saari, H.: The Ozone Monitoring Instrument, IEEE Transactions on Geoscience and Remote Sensing, 44, 1093–1101, 2006.

Lourens, A., Butler, T., Beukes, J. P., van Zyl, P. G., Beirle, S., Wagner, T., Heue, K.-P., Pienaar, J. J., Fourie, G. D., and Lawrence, M. G.: Re-evaluating the NO 2 hotspot over the South African Highveld, South African Journal of Science, 108, 1–6, 2012.

Magi, B. I., Hobbs, P. V., Schmid, B., and Redemann, J.: Vertical profiles of light scattering, light absorption, and single scattering albedo during the dry, biomass burning season in southern Africa and comparisons of in situ and remote sensing measurements of aerosol optical depths, Journal of Geophysical Research, 108, doi:10.1029/2002JD002361, http://www.agu.org/pubs/crossref/2003/2002JD002361.shtml, 2003.

Martin, R. V., Chance, K. V., Jacob, D. J., Kurosu, T. P., Spurr, R. J. D., Bucsela, E. J., Gleason, J. F., Palmer, P. I., Bey, I., Fiore, A. M., Li, Q., Yantosca, R. M., and Koelemeijer, R. B.: An improved retrieval of tropospheric nitrogen dioxide from GOME, Journal of Geophysical Research, 107, doi:10.1029/2001JD001027, http://www.agu.org/pubs/crossref/2002/2001JD001027.shtml, 2002.

McLinden, C. a., Fioletov, V., Boersma, K. F., Krotkov, N. A., Sioris, C. E., Veefkind, J. P., and Yang, K.: Air quality over the Canadian oil sands: A first assessment using satellite observations, Geophysical Research Letters, 39, n/a–n/a, doi:10.1029/2011GL050273, http://doi.wiley.com/10.1029/2011GL050273, 2012.

Mclinden, C. A., Fioletov, V., Shephard, M. W., Krotkov, N., Li, C., Martin, R. V., Moran, M. D., and Joiner, J.: Space-based detection of missing sulfur dioxide sources of global air pollution, Nature Geoscience, pp. 1–7, doi:10.1038/NGEO2724, 2016.

Platt, U. and Stutz, J.: Differential Optical Absorption Spectroscopy, Springer-Verlag, Berlin, Heidelberg, 1st edn., 2008.

Rhodes, B.: pyEphem Home Page, http://rhodesmill.org/pyephem/, 2015.

Richter, A., Burrows, J. P., Nüss, H., Granier, C., and Niemeier, U.: Increase in tropospheric nitrogen dioxide over China observed from space., Nature, 437, 129–32, doi:10.1038/nature04092, http://www.ncbi.nlm.nih.gov/pubmed/16136141, 2005.

Rozanov, V. V. and Rozanov, A. V.: Differential optical absorption spectroscopy (DOAS) and air mass factor concept for a multiply scattering vertically inhomogeneous medium: theoreti-

cal consideration, Atmospheric Measurement Techniques, 3, 751–780, doi:10.5194/amt-3-751-2010, http://www.atmos-meas-tech.net/3/751/2010/, 2010.

Rozanov, V. V., Rozanov, A. V., Kokhanovsky, A. A., and Burrows, J. P.: Radiative transfer through terrestrial atmosphere and ocean: Software package SCIATRAN, Journal of Quantitative Spectroscopy and Radiative Transfer, 133, 13–71, doi:10.1016/j.jqsrt.2013.07.004, http://dx.doi.org/10.1016/j.jqsrt.2013.07.004, 2014.

Stein, A. F., Draxler, R. R., Rolph, G. D., Stunder, B. J. B., Cohen, M. D., and Ngan, F.: Noaa's hysplit atmospheric transport and dispersion modeling system, Bulletin of the American Meteorological Society, 96, 2059–2077, doi:10.1175/BAMS-D-14-00110.1, 2015.

Streets, D. G., Canty, T., Carmichael, G. R., Foy, B. D., Dickerson, R. R., Duncan, B. N., Edwards, D. P., Haynes, J. A., Henze, D. K., Houyoux, M. R., Jacob, D. J., Krotkov, N. A., Lamsal, L. N., Liu, Y., Lu, Z., Martin, R. V., Gabriele, G. P., Pinder, R. W., Salawitch, R. J., and Wecht, K. J.: Emissions estimation from satellite retrievals : A review of current capability, Atmospheric Environment, 77, 1011–1042, doi:10.1016/j.atmosenv.2013.05.051, 2013.

Swap, R. J. and Tyson, P. D.: Stable discontinuities as determinants of the vertical distribution of aerosols and trace gases in the atmosphere, South African Journal of Science, 95, 63–71, 1999.

Toenges-Schuller, N., Stein, O., Rohrer, F., Wahner, a., Richter, A., Burrows, J. P., Beirle, S., Wagner, T., Platt, U., and Elvidge, C. D.: Global distribution pattern of anthropogenic nitrogen oxide emissions: Correlation analysis of satellite measurements and model calculations, Journal of Geophysical Research, 111, D05 312, doi:10.1029/2005JD006068, http://doi.wiley.com/10.1029/2005JD006068http://www.agu.org/pubs/crossref/2006/2005JD006068.shtml, 2006.

van der A, R. J., Eskes, H. J., Boersma, K. F., Noije, T. P. C. V., Roozendael, M. V., De Smedt, I., Peters, D. H. M. U., Meijer, E. W., van Noije, T. P. C., Van Roozendael, M., De Smedt, I., Peters, D. H. M. U., and Meijer, E. W.: Trends, seasonal variability and dominant NO x source derived from a ten year record of NO 2 measured from space, Journal of Geophysical Research, 113, 1–12, doi:10.1029/2007JD009021, http://www.agu.org/pubs/crossref/2008/2007JD009021.shtml, 2008.